Journal of Geophysical Research - Solid Earth

Supplementary Material of

The complex 4D multi-segmented rupture of the 2014 M_w 6.2 Northern Nagano Earthquake revealed by high-precision aftershock locations

Titouan Muzellec[(1)], Grazia De Landro[(1)],Giovanni Camanni[(2)], Guido Maria Adinolfi[(3)] and Aldo Zollo[(1)]

(1) Università degli Studi di Napoli "Federico II", Dipartimento di Fisica E. Pancini, RISSC-Lab, Naples, Italy

(2) Università degli Studi di Napoli "Federico II", DiSTAR, Naples, Italy

(3) Università degli Studi di Torino, Dipartimento di Scienze della Terra, Turin, Italy

Correspondence to: Titouan Muzellec (titouan.muzellec@unina.it)

Supplementary material

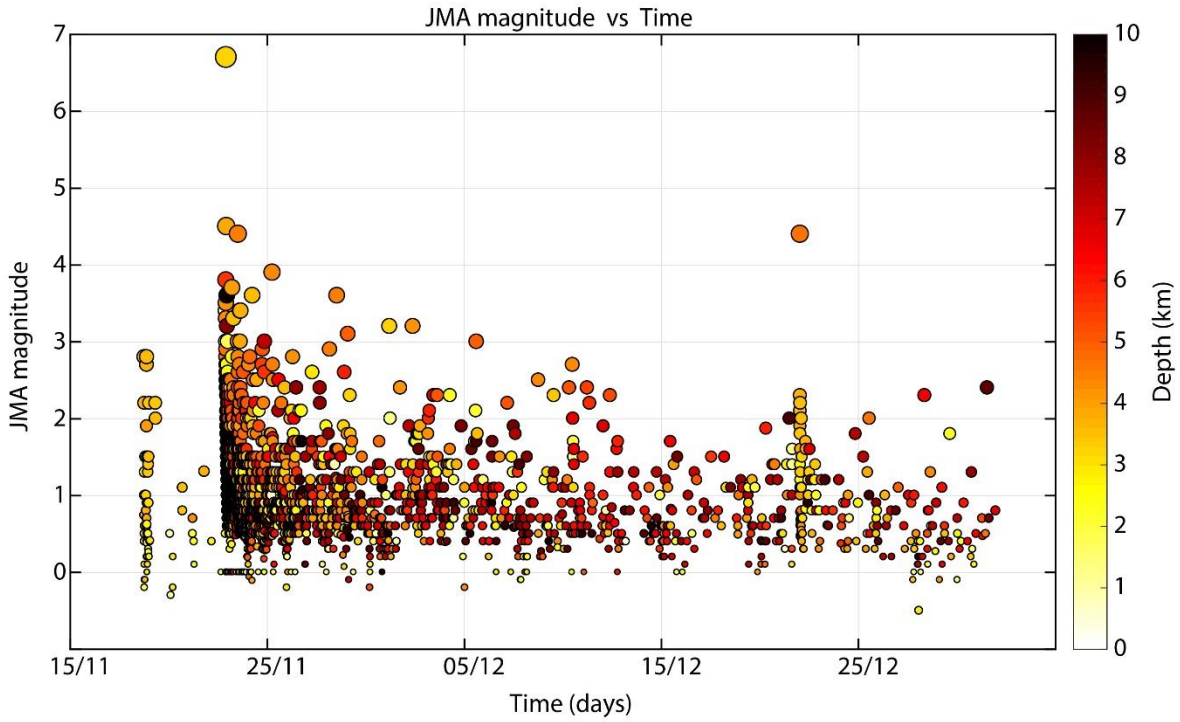

Fig. S1. Distribution of magnitude vs. time during the entire time period of the Northern Nagano sequence, i.e. from 15 November to 31 December 2014.

A1. Refinement procedure

Arrival-time refinement based on cross-correlation (CC) allows to calculate accurate differential travel-times for similar, co-located events. These CC differential times, indeed, depend on the event origin times and, in turn, on the quality of the initial location catalog. The differential travel times can be inverted directly for relative earthquake locations (e.g., Waldhauser and Ellsworth, 2000). In this case, accurate travel times difference estimated by cross-correlation for two events observed at one station can be attributed to the spatial offset between the events with high accuracy.

The refinement is applied on the three components independently at a single station by correlating events initially located in a 10 km square cube. The event selection for the correlation with respect to the initial location is done to avoid the correlation of events too far from each other. The seismic records were filtered between 1 Hz and 15 Hz with a bandpass filter and polarized by using the polarization filter defined by Ross and Ben-Zion (2014). The Single Value Decomposition method applied to the three ground motion components allows to estimate the eigen-value and the eigen-vectors to calculate the rectilinearity and the incidence angle with a sliding window of 1 s along the seismic records. Ross and Ben-Zion (2014) used the rectilinearity and the incidence angle to calculate the polarization filters for horizontal and vertical components. This filter removes at the best the S waves motion on the vertical component and the P waves motion on the horizontal components (Fig. 2a). Then the single station seismic records are correlated on the three components independently in a window of 0.5 s centered at the initial automatic picks to compute the correlation matrix. The waveform similarity classification is done with hierarchical clustering by considering a correlation coefficient threshold of 0.75 to define a family to which belong at least two seismic records (Fig. 2a). The waveforms not enough similar of the other events to be integrated into a family are considered as orphans and the refined pick is not considered.

By fixing a minimum number of events per family, we define a major trace for each family as the one with the higher signal-to-noise ratio (SNR). The correlation between all the seismic records of the family and the major event allowed us to estimate the shift and adapt the alignment between all the traces. Then a weighted stack based on the SNR and the polarity allows to get the reference trace (RT) for each family as proposed by Akram and Eaton (2016). The weighted stack allows to minimize the effect of the SNR and the polarity on the RT computation. The automatic picking algorithm is used on the RT of each family to compute the refined P and S picks by computing the characteristic function as the time derivative of the Kurtosis parameter. The refined pick estimated on the RT corresponds to the new pick for all the aligned traces of the same family (Fig. 2a). The comparison of the amplitude ratio before and after the picks (initial and refined one) allows to clearly show the improvement of the arrival time estimation by increasing the amplitude ratio with the refined picks (Fig. S2). The catalogs consist

of (1) 41821 P and 37494 S readings corresponding to 2477 earthquakes. By applying the refinement picking procedure, 36563 P and 35472 S picks are refined giving around 90% of the picks of Nagano dataset.

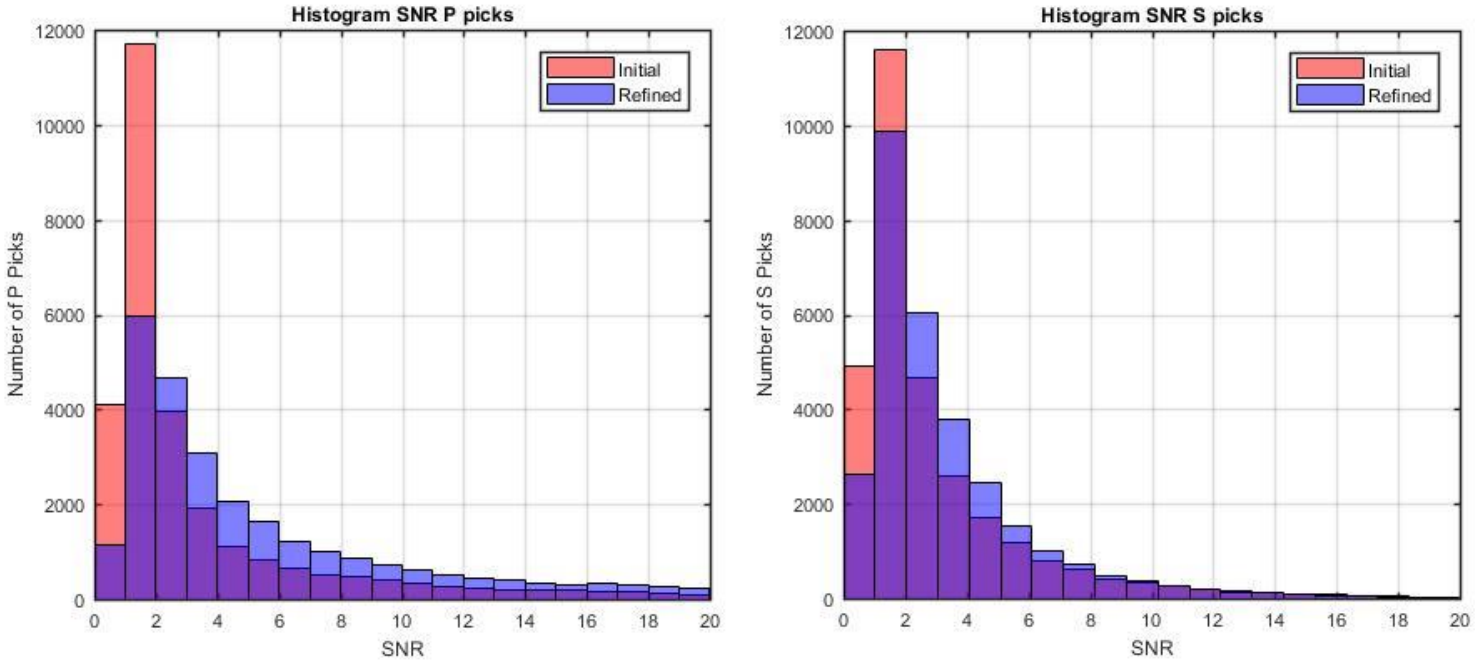

Fig. S2. Comparison between Signal to noise ratio measured from initial and refined picks for a subset of events of Nagano sequence. The SNR is calculated on windows of 0.5 seconds before and 0.5 seconds after the picks. It is clearly visible the increase of SNR associated with refined picks, as a confirmation to the picking quality improvement.

A2. Location strategy

Tomographic inversion

In order to determine the 3D P- and S-wave velocity models, the refined travel-time dataset was inverted by applying an iterative, linearized, tomographic approach (Latorre et al., 2004). Due to the source-station configuration we have investigated a volume of 100×120×18 km^3, discretized with a grid of regularly spaced nodes 10×10×3 km^3.We started from the 1D initial model of JMA. We selected the damping parameter using an empirical approach, by performing several inversions with different values. The selected damping parameters are the ones providing the best compromise between the variance reduction of the residuals and the increase of the solution variance. By inspecting the trade-off curves retrieved for each parameterization, the value of 0.3 was selected for all the parameterizations. To assess the resolution of final velocity model, we computed the derivative weight sum (DWS), which measures the ray density in the neighborhood of every node (Hauksson and Shearer, 2006) and ensured that the volume interested by the sequence is well resolved up to 10 km of depth). On both revised P- and S-wave velocity model, there is a strong variation of velocity along the strike of the OTNF and KF fault system bounding two units. In first the kilometers depth, the domain on the west side of the fault system is characterized by relatively high P- (5 – 5.75 km/s) and S-wave (2.75 – 3.5 km/s) velocities, while the domain on the east side of the fault system is characterized by relatively low P- (4.5 – 5 km/s) and S-wave (2.5 – 3 km/s) velocities. By looking the map view of the velocity models, this strong east-west variation of velocity is no longer evident at 7 km depth. The geological structure related to the low velocity zone should end between 4 and 7 km depth. By comparing the position of the velocity anomalies and the geological features at the surface, the low velocity anomaly on the east side of the fault system is related to the NFM basin while the high velocity anomaly of the west side of the fault corresponds to the INZ (basement structure).

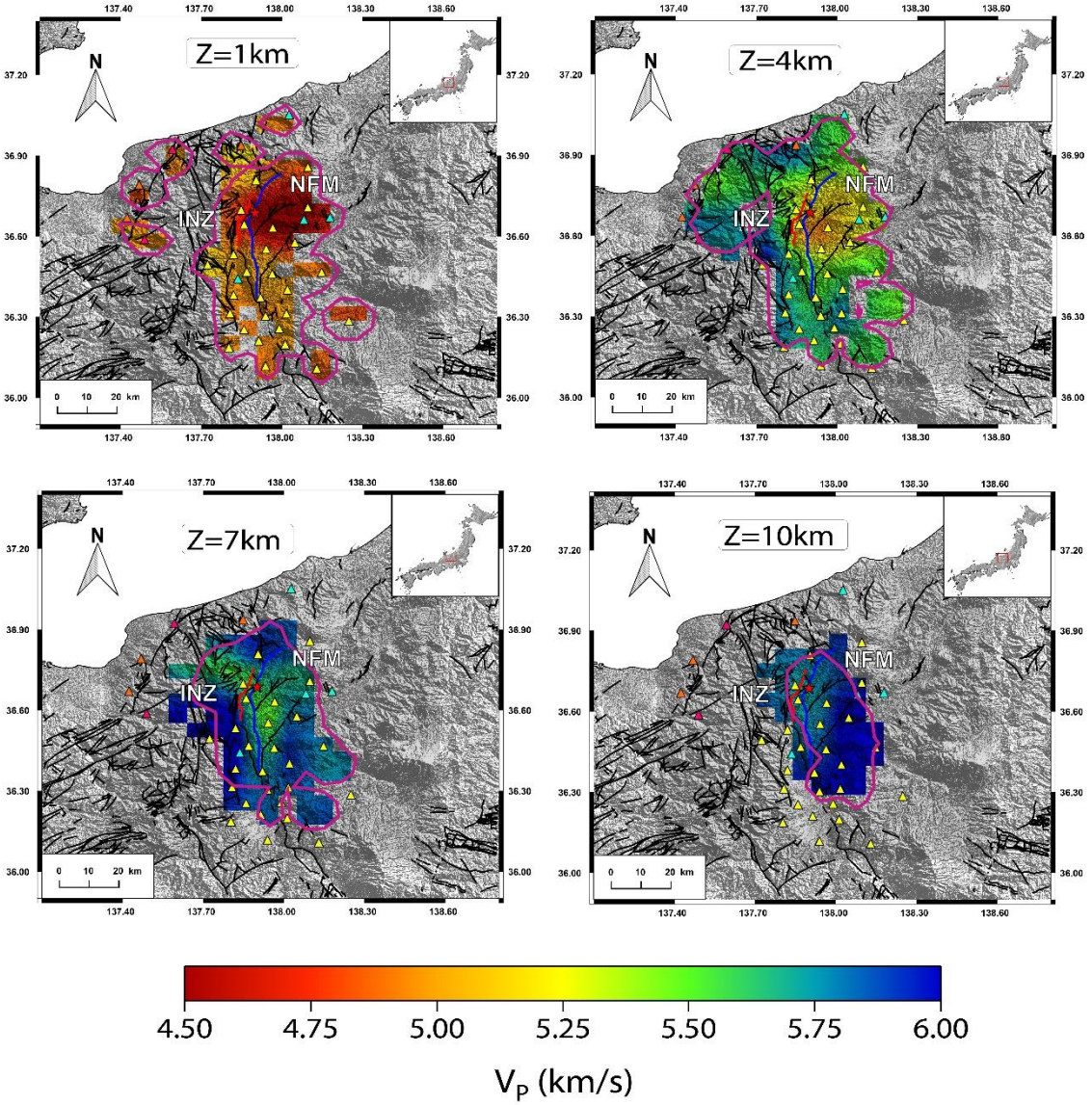

Fig. S3.1 P-wave velocity model. The contour line in pink corresponds to the derivative of weight sum (DWS), which is a weighted measure of the total ray length through a node in the inversion grid, of about 10 000.

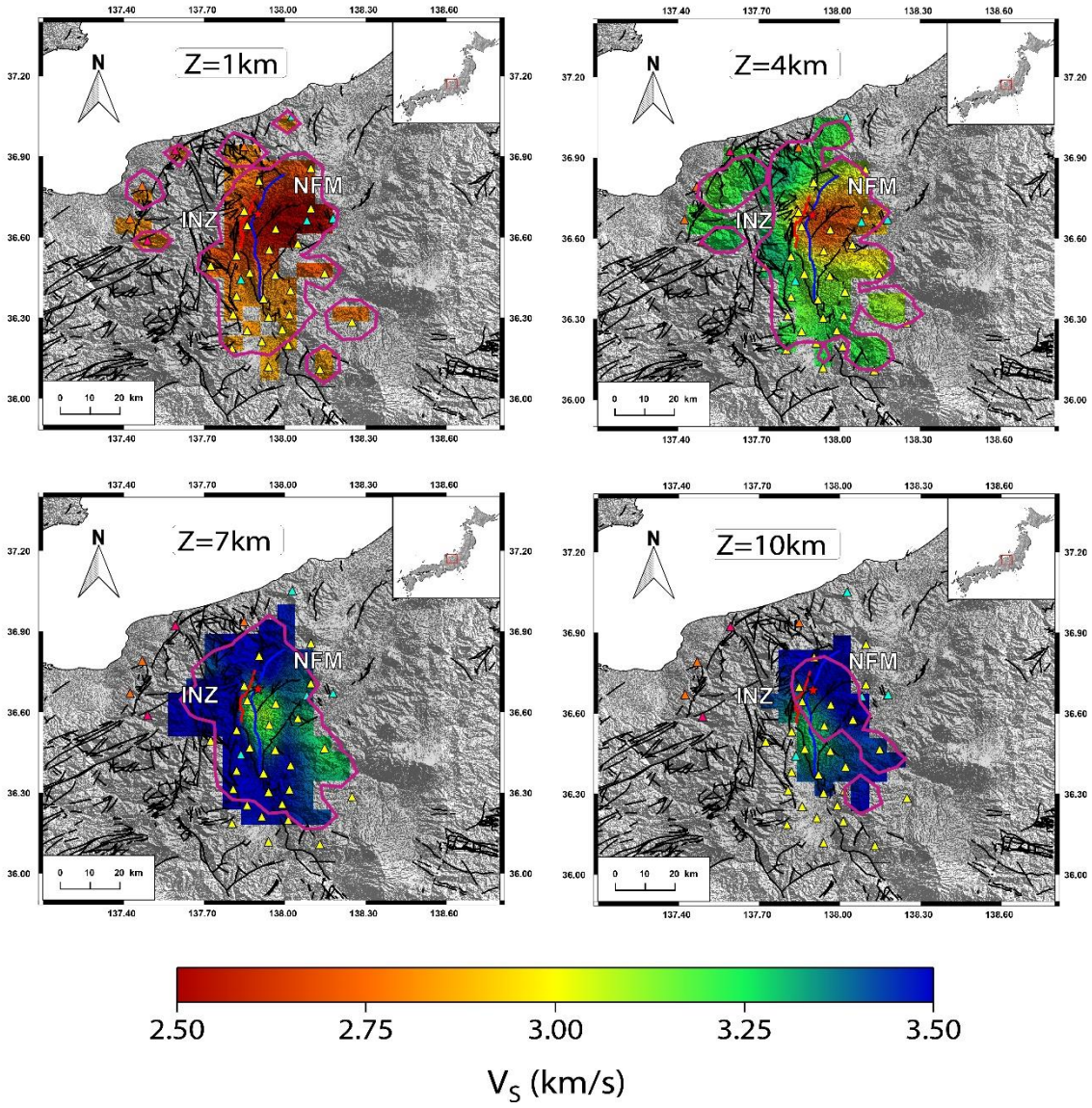

Fig. S3.2 S-wave velocity model. The contour line in pink corresponds to the derivative of weight sum (DWS), which is a weighted measure of the total ray length through a node in the inversion grid, of about 10 000.

DD Location

To minimize the residuals for pairs of earthquakes at the single station, we combined the ordinary phase picks information from the catalog data and the high precision differential travel

time from phases picking refinement based on cross-correlation for the double difference location procedure with HypoDD (Waldhauser and Ellsworth, 2000). To compute the travel time difference from the catalog data, we used a maximum separation distance of 10 km. This condition resulted in 567,779 linked event pairs that produced 3,852,203 differential P-phase and 2,489,092 differential S-phase absolute travel times. We used the families from the refinement procedure to define the couple of events to compute the relative travel-time difference. It resulted in 222,698 linked event pairs that produced 1,830,032 differential P-phase and 1,049,378 differential S-phase relative travel times. We then proceeded relocating the hypocenters iteratively following the weighting scheme described below. We started the ratio of relative to absolute time with 0.01 for the first 7 iterations and progressively weighted the relative times higher, 1.0 in the last 9 iterations. This process resulted in a 30% reduction of the weighted rms residuals from 0.112 s (mean rms with refined picks and 3D velocity model) to 0.034 s.

To estimate the error from the DD location procedure, we used the SVD inversion method on a selection of 741 events among the different clusters. The couple of events, for the SVD inversion, are defined with respect to a maximum distance of 1.5 km. This maximum distance will induce a lower number of linked event pairs and differential travel-times inducing an overestimation of the location error with respect to an inversion with a higher number of event pairs. Fig. S4 shows the histograms of the location errors (vertical and horizontal) estimated by DD location with the SVD inversion, the location error from absolute location in a 1D with the initial picks, and the location error from absolute location in a 3D with the refined picks. The double difference procedure significantly reduces the location error with an average error of about 140 m with respect the absolute location error with an average error of about 190 m in a 3D model and 580 m in a 1D model.

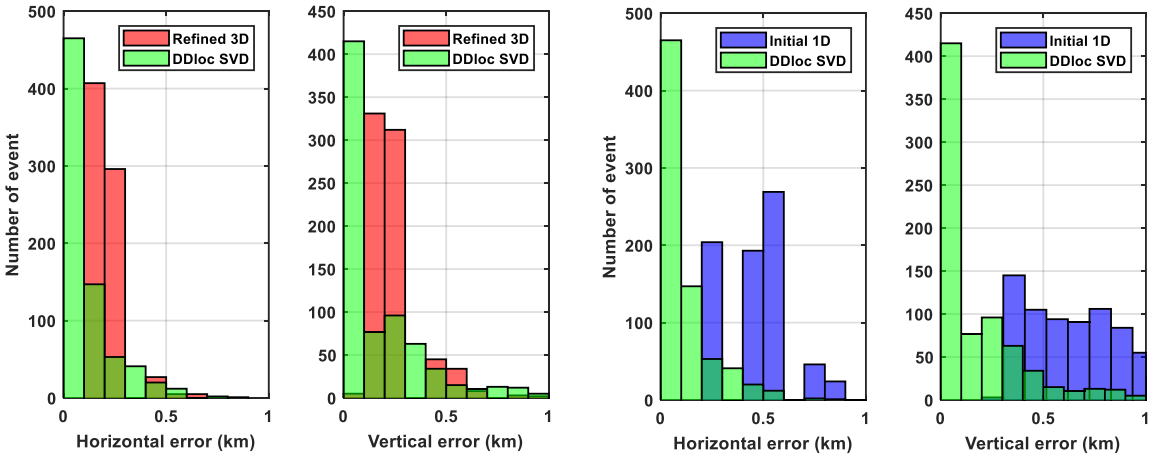

Fig. S4. Histogram of the location errors.

A3. Rupture directivity

The method proposed by Convertito et al, (2012) assumes a line-source rupture occurring in a homogeneous velocity model to estimate the maximum likelihood parameters of the kinematic source model through the modeling of the peak motion amplitude modulated by a directivity factor (Boatwright, 2007):

$$C_d = \frac{1}{2}\sqrt{\frac{(1+e)^2}{(1-\alpha cos\theta)^2}+\frac{(1-e)^2}{(1+\alpha cos\theta)^2}} \quad (1)$$

where $\alpha = \frac{V_R}{\beta}$ is the Mach number (V_R is the rupture velocity, β is the shear wave velocity), θ is the angle between the ray leaving the source and the direction of rupture propagation, and e is the coefficient accounting for the percent of the unilateral rupture $e = \frac{2L'-L}{L}$, where L' and L are the prevalent and total rupture lengths, respectively. The fault is assumed to be rectangular with two adjacent rectangles, a prevalent and a secondary one, expanding from the hypocenter location.

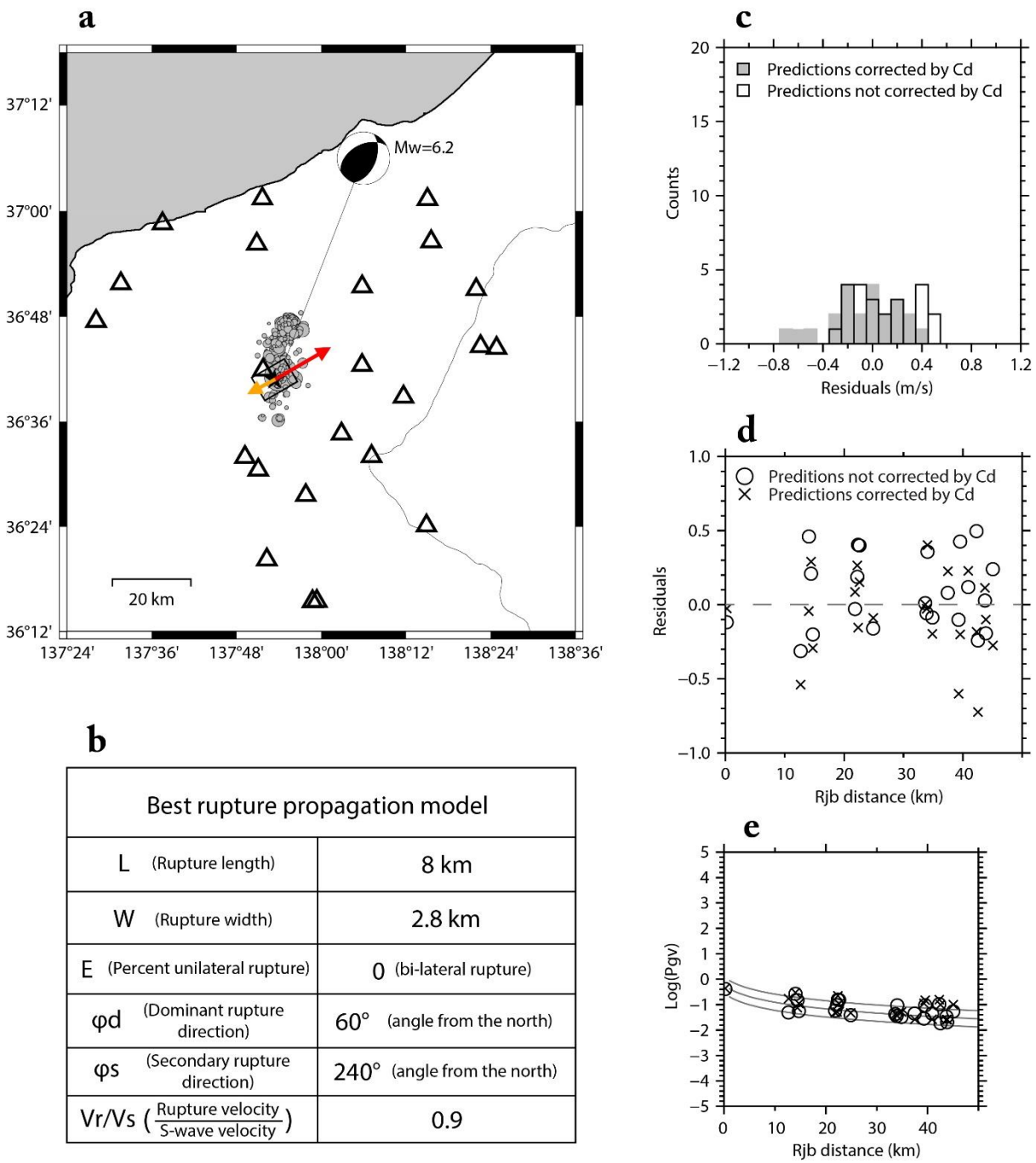

b

Best rupture propagation model	
L (Rupture length)	8 km
W (Rupture width)	2.8 km
E (Percent unilateral rupture)	0 (bi-lateral rupture)
φd (Dominant rupture direction)	60° (angle from the north)
φs (Secondary rupture direction)	240° (angle from the north)
Vr/Vs ($\frac{\text{Rupture velocity}}{\text{S-wave velocity}}$)	0.9

Fig S5. Rupture directivity analysis (a) map view of the first 3 hours aftershocks and the surface projection of the main (red) and secondary (orange) rupture directions (arbitrary arrow lengths); (b) the list of output parameters of the best inverted rupture model (see Convertito et al., 2012); (c) Histogram of the residuals $\log(PGV_{obs})$-$\log(PGV_{predicted})$; (d) Residual distribution vs the Joyner-Boore distance (R_{jb}), e.g. the closest epicentral distance from the fault area projected at the Earth surface; (e) Log-log plot of the peak ground velocity (PGV) as

function of the Joyner-Boore distance, along with the theoretical values (continuous curves) as determined from the Kanno et al. (2006) GMPE for Japan for M_w 6.2 earthquake.

A4. Composite focal mechanism

Table S1. Composite Focal mechanisms of significant clusters

	Strike (°)	Dip (°)	Rake (°)	Strike uncertainty (°)	Dip uncertainty (°)	Rake uncertainty (°)
Cluster A	20	55	60	5	3	10
Cluster B	47	61	163	5	18	5
Cluster C	20	50	80	5	10	0
Cluster D	210	60	160	8	15	10
Cluster E	70	80	150	3	8	25
Cluster F	254	61	168	3	3	5
Cluster G	206	77	-82	18	18	15
Cluster H	16	77	52	5	15	15
Cluster I	20	80	20	10	8	25

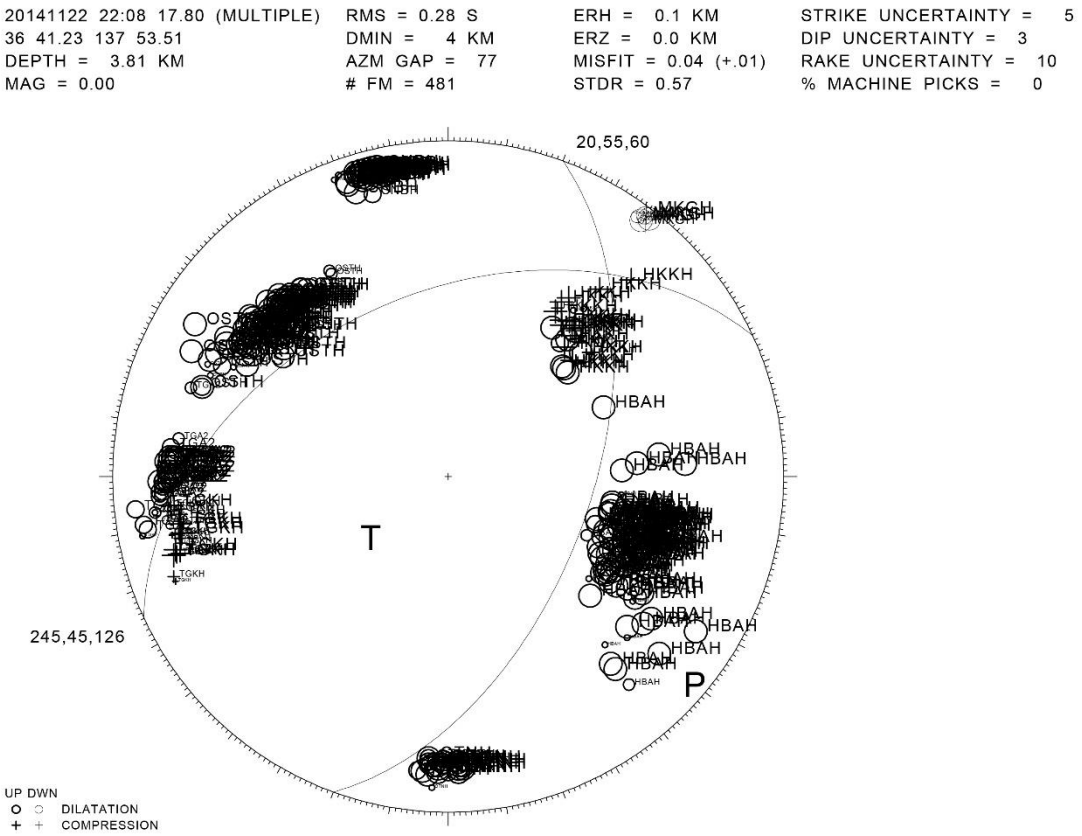

161

162 **Fig S6.** Focal mechanism estimation for cluster A

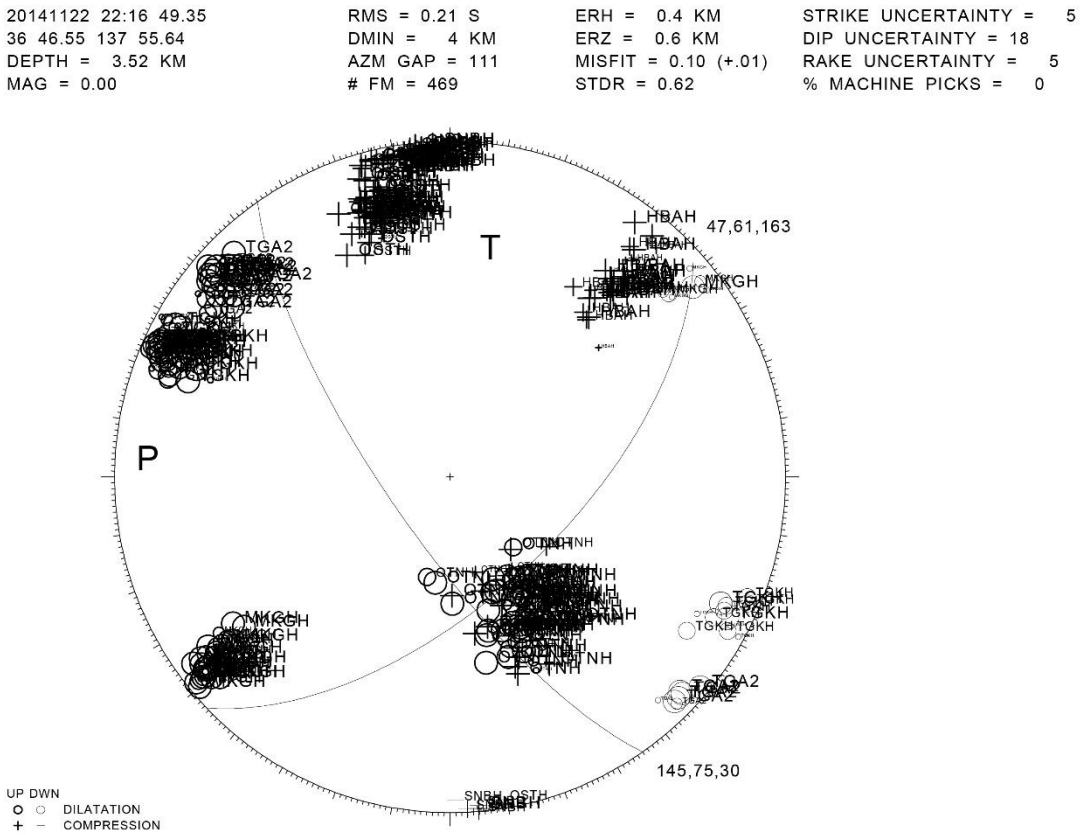

163

164 **Fig S7.** Focal mechanism estimation for cluster B

165

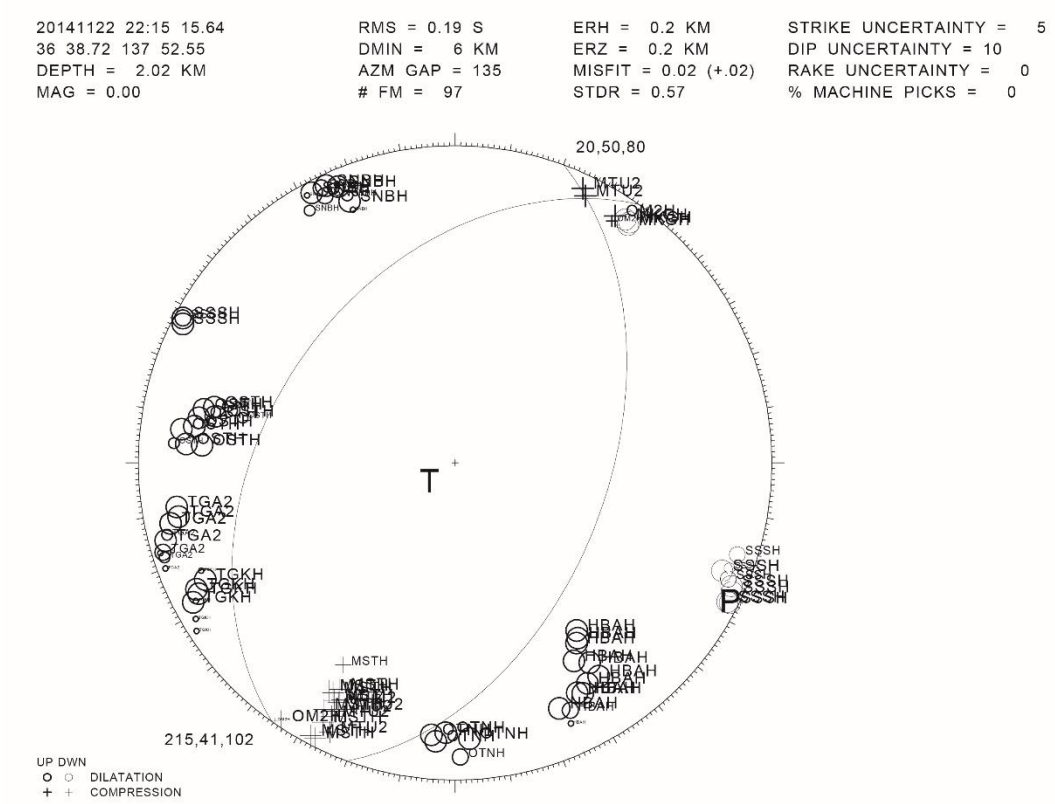

166 **Fig S8.** Focal mechanism estimation for cluster C

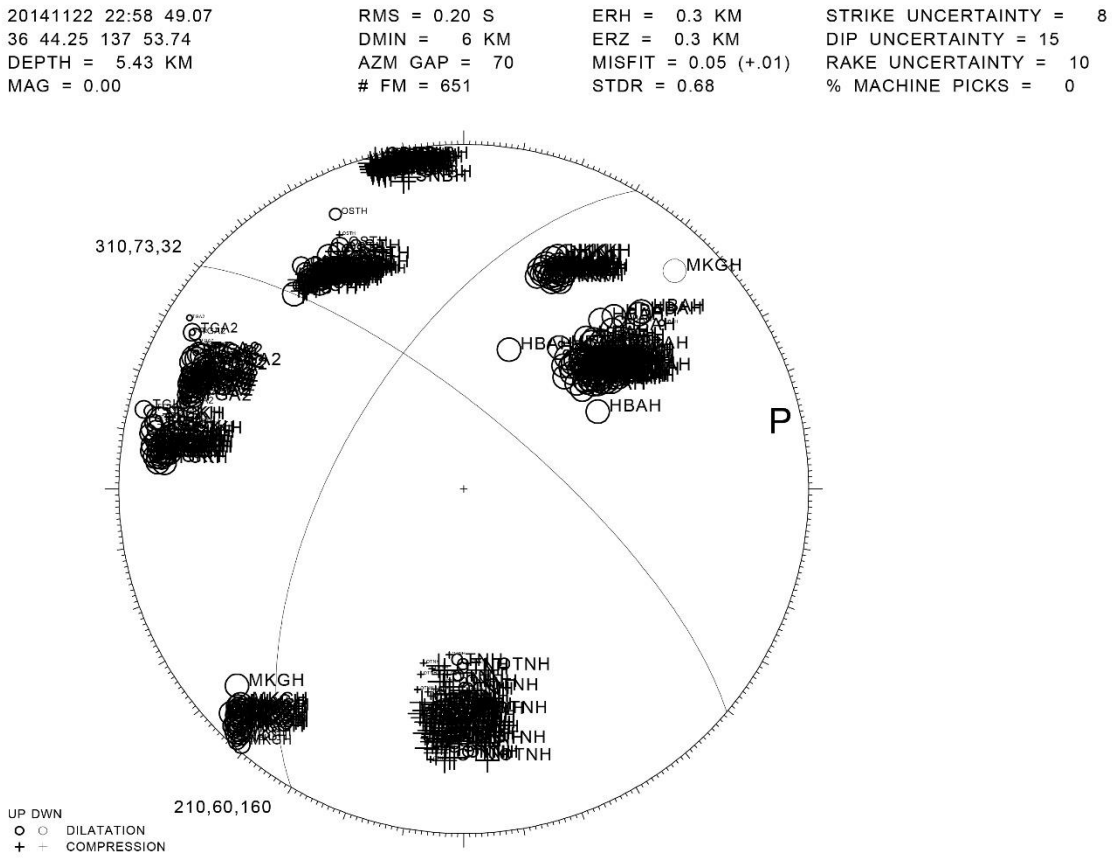

167

168 **Fig S9.** Focal mechanism estimation for cluster D

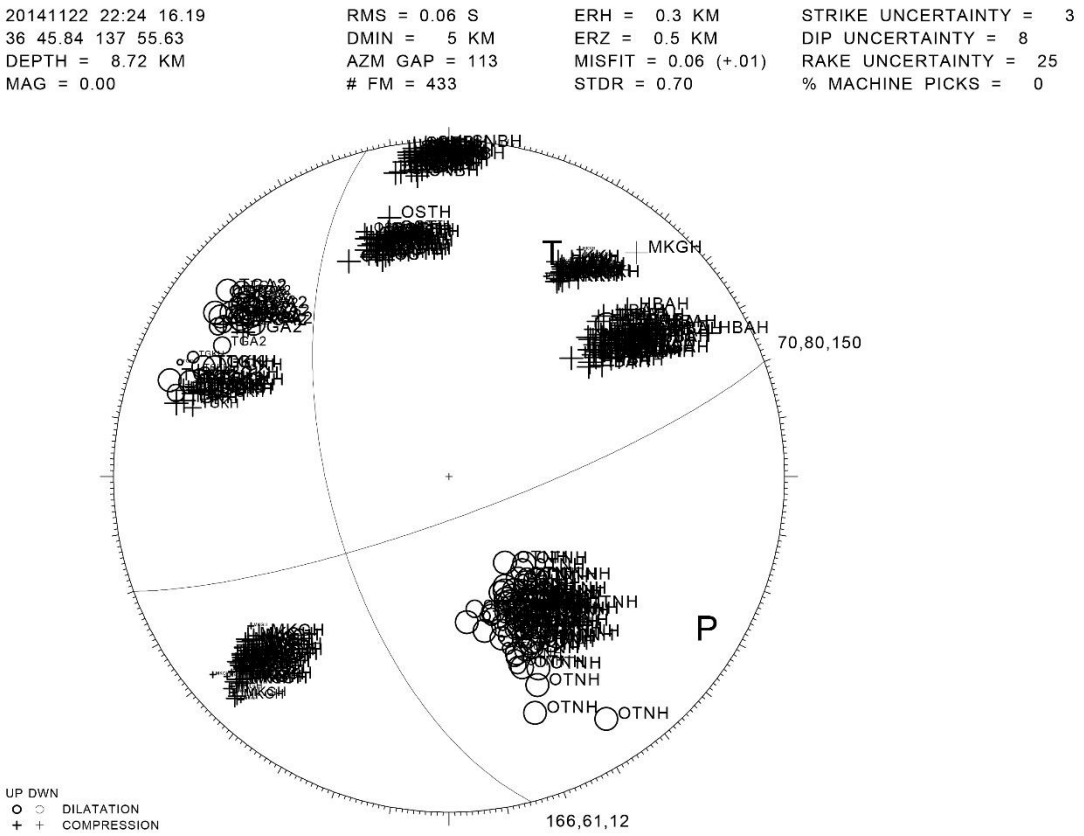

169

170 **Fig S10.** Focal mechanism estimation for cluster E

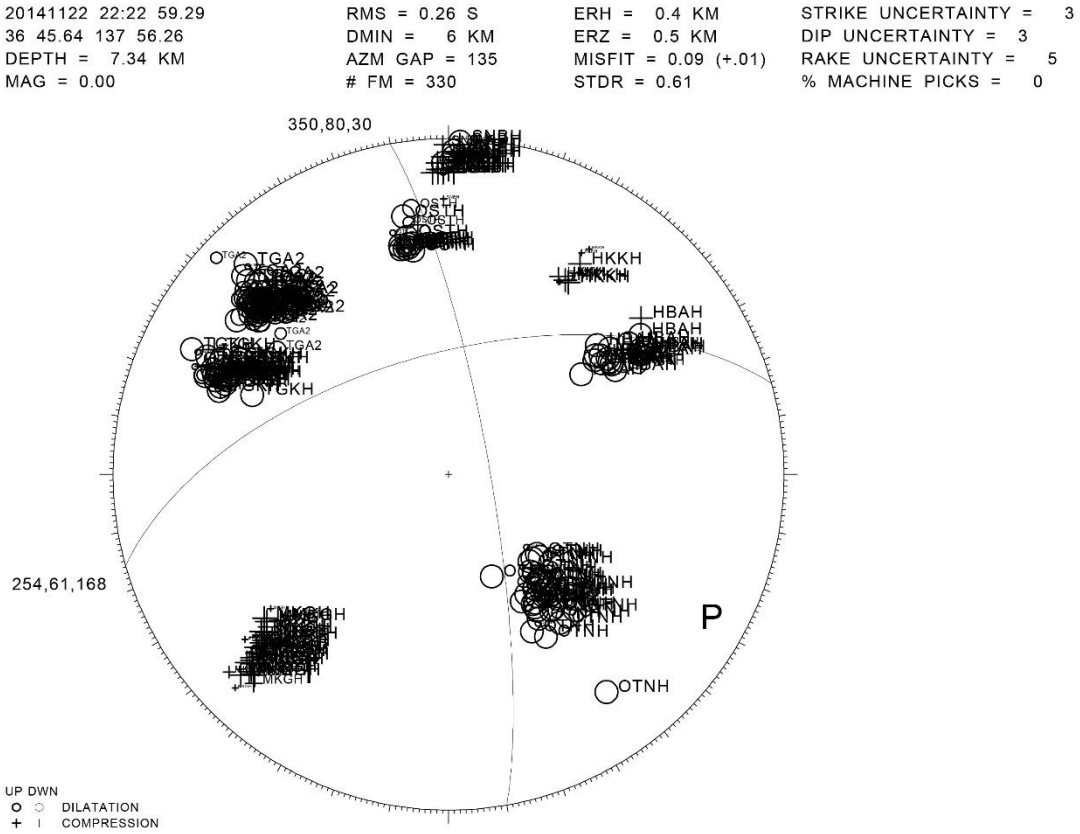

171

172 **Fig S11.** Focal mechanism estimation for cluster F

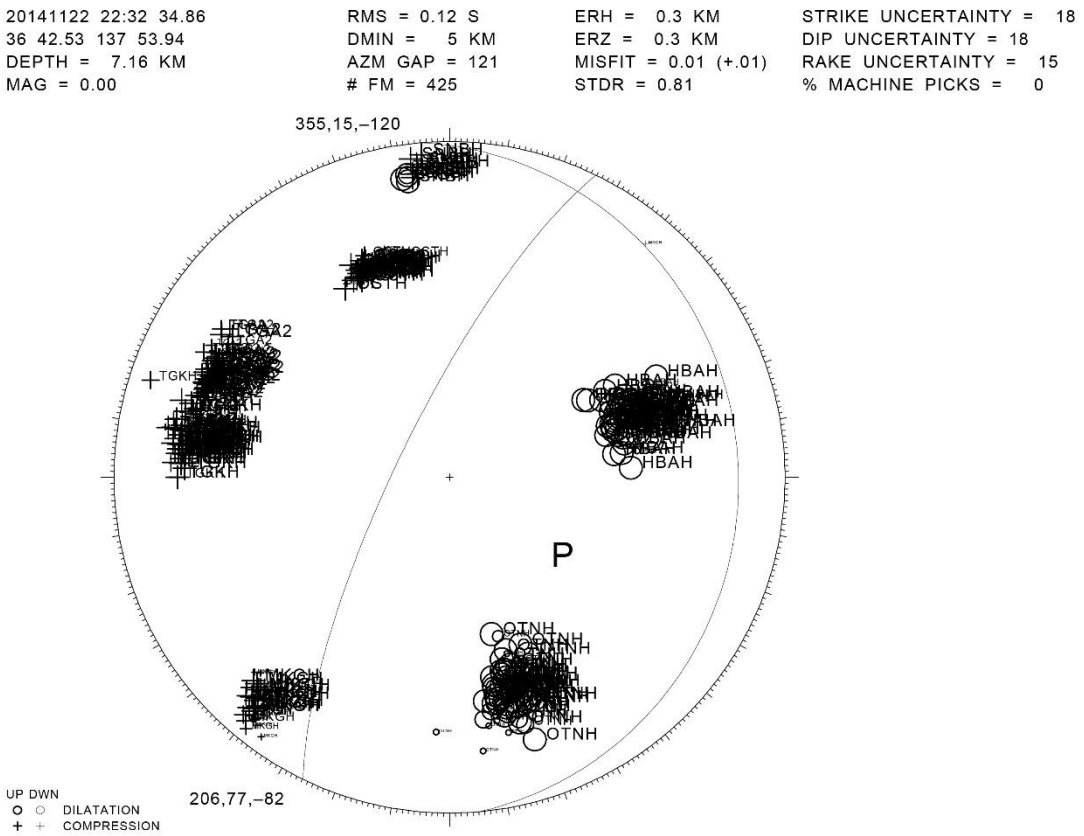

173

174 **Fig S12.** Focal mechanism estimation for cluster G

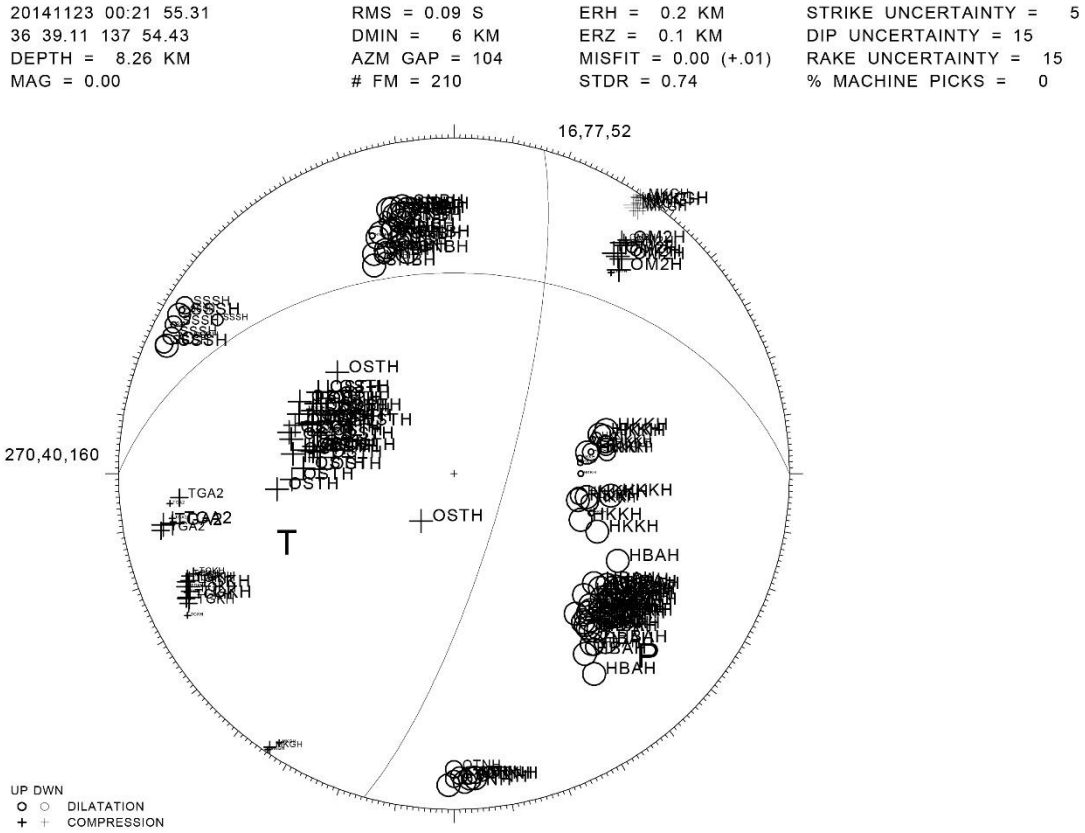

175

176 **Fig S13.** Focal mechanism estimation for cluster H

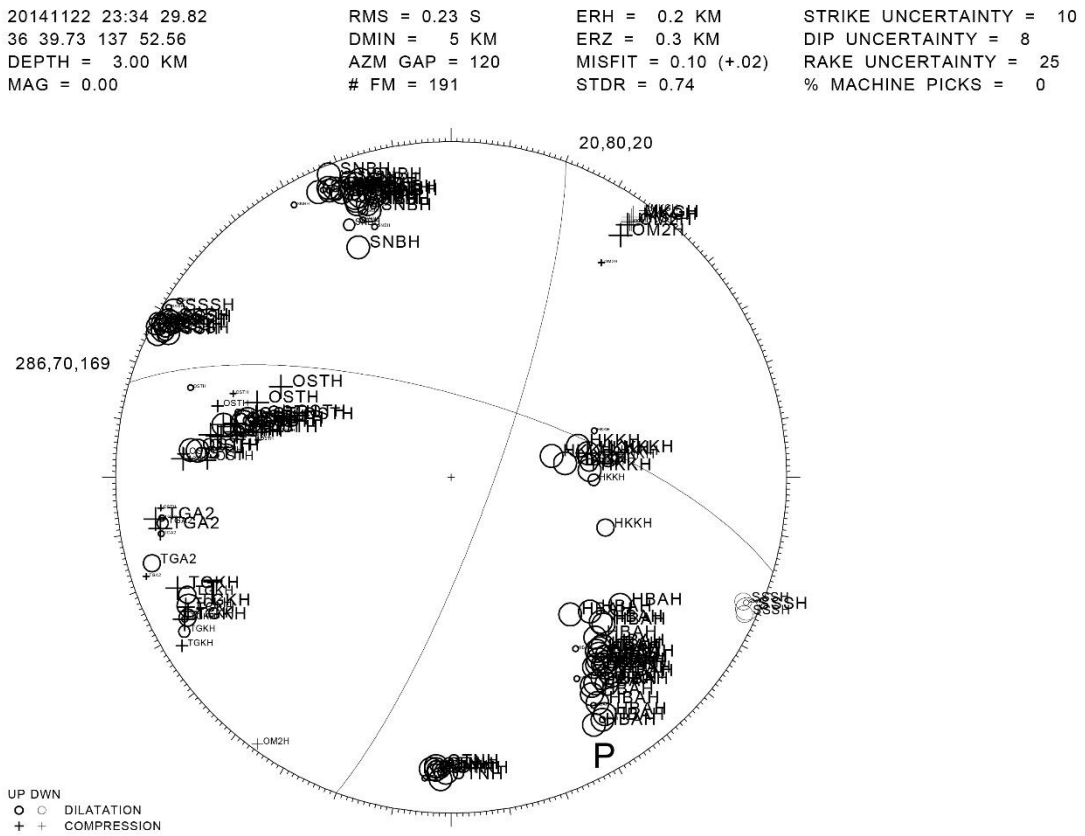

177

178 **Fig S14.** Focal mechanism estimation for cluster I

A5. Slip model (Kobayashi et al., 2018)

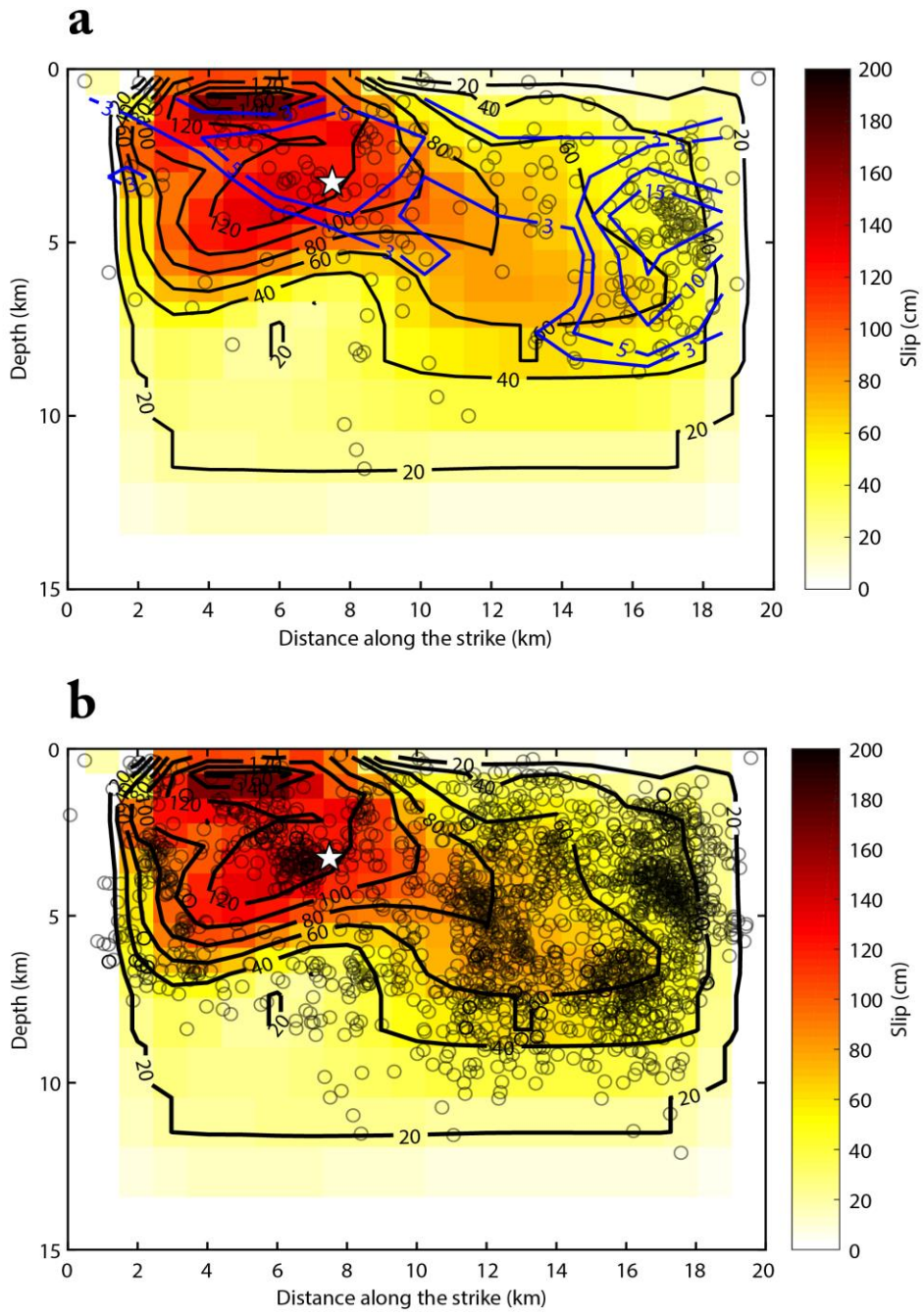

Fig S15. Projected aftershock seismicity of (a) the first 3 hours (b) the entire time period on the slip model obtained by Kobayashi et al., 2018. Black circles indicate the aftershock location. The black and blue lines indicate the contour of the slip along the fault and the seismicity density, respectively.

A6. Cluster selection and cumulative seismicity

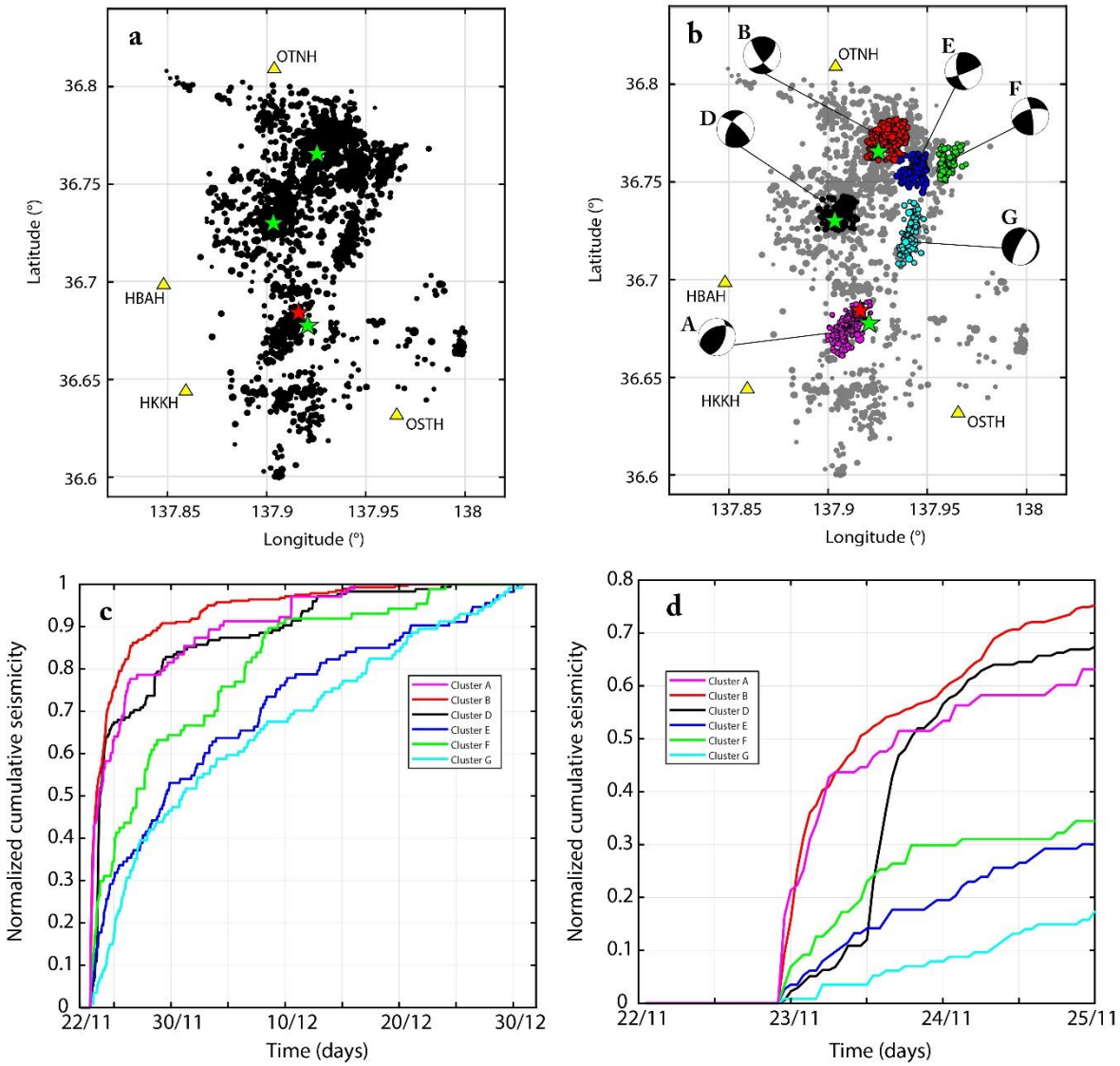

Fig. S16. Map view (a) of the whole seismicity over the entire time period and (b) the selected clusters with (c-d) normalized cumulative seismicity in time. The index letters of each composite focal mechanism are referred in the Table S1.